

End-to-end Optimization of Optical Communication Systems based on Directly Modulated Lasers

SERGIO HERNANDEZ^{1,*}, CHRISTOPHE PEUCHERET², FRANCESCO DA ROS¹, AND DARKO ZIBAR¹

¹Department of Electrical and Photonics Engineering, Technical University of Denmark, 2800 Kongens Lyngby, Denmark

²Univ. Rennes, CNRS, FOTON - UMR6082, 22305 Lannion, France

*shefe@dtu.dk

Compiled May 17, 2024

The use of directly modulated lasers (DMLs) is attractive in low-power, cost-constrained short-reach optical links. However, their limited modulation bandwidth can induce waveform distortion, undermining their data throughput. Traditional distortion mitigation techniques have relied mainly on the separate training of transmitter-side pre-distortion and receiver-side equalization. This approach overlooks the potential gains obtained by simultaneous optimization of transmitter (constellation and pulse shaping) and receiver (equalization and symbol demapping). Moreover, in the context of DML operation, the choice of laser-driving configuration parameters such as the bias current and peak-to-peak modulation current has a significant impact on system performance. We propose a novel end-to-end optimization approach for DML systems, incorporating the learning of bias and peak-to-peak modulation current to the optimization of constellation points, pulse shaping and equalization. The simulation of the DML dynamics is based on the use of the laser rate equations at symbol rates between 15 and 25 Gbaud. The resulting output sequences from the rate equations are used to build a differentiable data-driven model, simplifying the calculation of gradients needed for end-to-end optimization. The proposed end-to-end approach is compared to 3 additional benchmark approaches: the uncompensated system without equalization, a receiver-side finite impulse response equalization approach and an end-to-end approach with learnable pulse shape and nonlinear Volterra equalization but fixed bias and peak-to-peak modulation current. The numerical simulations on the four approaches show that the joint optimization of bias, peak-to-peak current, constellation points, pulse shaping and equalization outperforms all other approaches throughout the tested symbol rates.

<http://dx.doi.org/10.1364/ao.XX.XXXXXX>

1. INTRODUCTION

Directly modulated lasers (DMLs) are a compelling option for short-reach intensity modulation/direct detection (IM/DD) systems, thanks to their low energy consumption, small form factor and reduced cost [1, 2]. The aim in such systems is to maximize the symbol rate R_s while maintaining sufficient optical received power P_{rec} in order to increase net data throughput. This requires the laser to operate in the large-signal regime, where the high modulation index allows high extinction ratio and peak-to-peak output power. However, the large-signal DML dynamics introduce significant waveform distortions, potentially resulting in nonlinear intersymbol interference as the symbol rate is increased [3, 4]. This is due to the modulation-induced changes in carrier and photon concentration within the laser active region, that cause nonlinear memory effects in the output optical field. Consequently, the DML's response time sets a limit on its modulation bandwidth, restricting the laser's throughput [5].

Although increasing the bias current to the laser can enhance modulation bandwidth, it comes at the expense of increased energy consumption and lower extinction ratio, resulting in a receiver power penalty. Another alternative to partially overcome bandwidth limitations is tuning transmitter (TX), receiver (RX), digital signal processing (DSP) and the laser-driving configurations (bias and peak-to-peak current to the laser) separately. Yet, the large amount of parameters to be optimized within the DSP pipeline (pulse shaping, pre-distortion, receiver-side equalization) may require a high amount of simulation/system evaluations to converge towards optimal configurations, making such approach intractable in cases where such evaluations are time consuming.

Recent advances in DML development have focused on delivering >100 Gbps bit rates with low energy consumption (<1 pJ/bit) through the use of coupled-cavity laser structures [6–8]. The additional optical feedback enabled by such structures en-

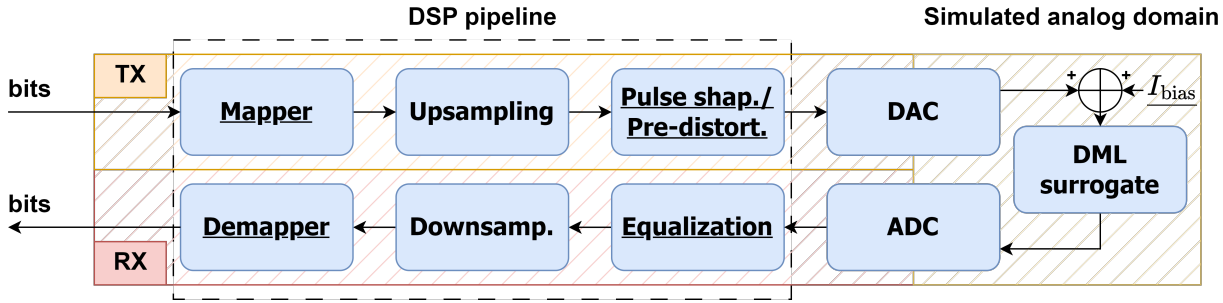


Fig. 1. Proposed numerical simulation of a back-to-back DML system. The DSP pipeline at TX (green) and RX (red) aims to encode and decode information subject to the constraints imposed by the simulated analog domain (yellow). The elements optimized in this work are underlined

ables higher modulation bandwidths through the use of photon-photon resonance (PPR) and detuned loading. Impairment compensation in DML-based systems [1, 9] has however relied mainly on separate transmitter-side pre-distortion and receiver-side optimization, omitting the potential gains of optimizing both TX and RX jointly. This arises from the fact that the large-signal DML dynamics are governed by nonlinear differential equations, hindering the calculation of analytical gradients and therefore the simultaneous optimization of transmitter and receiver using standard gradient-based optimization techniques. An accurate, differentiable model of the DML dynamics can prove useful in this scenario, allowing the propagation of gradients between TX and RX while accounting for the DML-induced signal impairments. Data-driven modeling is a viable option in this context provided that sufficient data is available, yet the choice of model structure (Volterra filters, neural networks) can pose a challenge. In [10], we conduct a comparison between model structures using the laser rate equations as source of DML waveform data. The results show the potential of transformer-based neural networks [11] in the prediction of the DML dynamics.

DSP algorithms have extensively been used to compensate for transmission impairments within optical communication systems. End-to-end (E2E) learning has attracted a special interest in this scope, as it enables the simultaneous optimization of TX (constellation and pulse shaping) and RX, given that a differentiable model of the system under test is available [12, 13]. Through the use of alternative approaches like gradient-free optimization and reinforcement learning, it is also possible to avoid modeling the communication channel and use local gradient approximations [14, 15]. The focus in E2E learning is to substitute one or several functions of the DSP pipeline at both ends of the channel by an adaptive optimizable function [16]. Autoencoders (AEs) are especially popular in this context, as they allow the compression and decompression of data [17] in a similar fashion to how communication systems map symbols to optical waveforms and viceversa [16]. Approaches such as geometric constellation shaping (GCS), that have become standard in state-of-the-art in long-haul coherent systems, can be implemented based on this principle [15, 18–21].

In this paper, we demonstrate E2E optimization of TX and RX DSP, together with bias and peak-to-peak modulation current for impairment compensation of DML systems. The proposed simulation approach is shown in Fig. 1. The modeling of the DML dynamics is performed using a data-driven surrogate model, based on the numerical solution of the rate equations as source of data. The waveform data generation uses 4-level pulse amplitude modulation (4PAM) symbols in a back-to-back (B2B)

simulation. The proposed AE-based approach is used to optimize DSP configurations at TX (GCS, pulse shaping) and RX (equalization, symbol detection) simultaneously. In addition, the input current offset I_{bias} and the peak-to-peak modulation current I_{pp} are used as learnable parameters. This provides insight on the optimal compromise between extinction ratio and distortion of the optical waveform. Additionally to the AE approach, three more approaches are included as a benchmark: the uncompensated system without equalization, a receiver-side linear feed-forward equalizer (FFE) and a second E2E approach with learnable pulse shape (LPS) and RX-side Volterra nonlinear equalization (VNLE), but excluding I_{bias} and I_{pp} from the optimization. The results show the advantage of the joint optimization of bias, modulation current and DSP for DML systems, with the AE yielding performance gains over the RX-only equalization and a considerable advantage over the VNLE setup in terms of symbol error rate (SER) and mutual information (MI).

This paper is structured as follows: Section 2 describes the dynamic behaviour of DMLs and the state-of-the-art in optical communication laser development. Section 3 analyzes the available algorithms for the modeling of DMLs in terms of complexity, interpretability and compatibility with gradient-based optimization. The fundamentals of E2E learning and its application to DMLs in the literature is reviewed in Section 4. The motivation and structure of the proposed DML model and the optimization approach around it can be found in Section 5. The results of the E2E-optimized B2B DML system simulation are described in Section 6. The conclusions are summarized in Section 7.

2. DML DYNAMICS

The rate equations governing the photon density $S(t)$, carrier density $N(t)$ and phase $\phi(t)$ in DMLs are given by [5]:

$$\frac{dS(t)}{dt} = \Gamma g_0 (N(t) - N_0) \frac{1}{1 + \epsilon S(t)} S(t) - \frac{S(t)}{\tau_p} + \frac{\Gamma \beta N(t)}{\tau_n}, \quad (1)$$

$$\frac{dN(t)}{dt} = \frac{I(t)}{qV} - \frac{N(t)}{\tau_n} - g_0 (N(t) - N_0) \frac{1}{1 + \epsilon S(t)} S(t), \quad (2)$$

$$\frac{d\phi(t)}{dt} = \frac{1}{2} \alpha \left[\Gamma g_0 (N(t) - N_0) - \frac{1}{\tau_p} \right], \quad (3)$$

where Γ is the mode confinement factor, g_0 is the gain slope constant, N_0 is the carrier density at transparency, ϵ is the gain compression factor, τ_p is the photon lifetime, β is the fraction of spontaneous emission coupled into the lasing mode, τ_n is

the electron lifetime, $I(t)$ is the injected current, q is the electron charge, V is the active layer volume and α is the linewidth enhancement factor. The output optical power is given by:

$$P(t) = \frac{S(t)V\eta_0 h\nu}{2\Gamma\tau_p}, \quad (4)$$

where η_0 is the differential quantum efficiency, h is Planck's constant, and ν is the unmodulated optical frequency. Thus, the modulated optical power $P(t)$ is proportional to the photon density $S(t)$, while the rate of change of the optical phase (instantaneous angular frequency) is proportional to the carrier density over threshold.

A. Small-signal regime

The term $N(t) - N_0$ in Eq. (1) and (2) hints the reservoir-like behaviour of the carrier density fluctuation in the laser active region. When I reaches the laser's threshold current level I_{th} (optical gain overcomes cavity losses) the carrier density reaches its maximum steady-state level N_0 (the reservoir becomes full). The carrier excess generated by $I - I_{th}$ "overflows" the reservoir, generating net stimulated emission of photons. The higher $I - I_{th}$ is, the more photons are emitted, and through Eq. (4) the larger $P(t)$ will be. This also entails that the stimulated recombination of carriers increases, bringing $N(t)$ back to its threshold level N_0 after some transient period. The interaction between carriers and photons creates a damped oscillatory behaviour in $S(t)$ and $N(t)$ (carrier-photon resonance) when $I(t)$ is modulated, as the increase of one drives the decrease of the other until steady state is reached. The optical gain generated by the laser, dependent of $N(t)$ and $S(t)$, is given by Eq. (5):

$$g(N, S) = \frac{g_0}{1 + \epsilon S(t)} \ln \left(\frac{N(t) + N_s}{N_0 + N_s} \right), \quad (5)$$

where N_s is a fitting parameter used to ensure the logarithm is finite and defined for $N(t) > 0$. Both g_0 and N_s are usually fitted from the measured response of the laser [22]. Given that the optical gain g is monotonically (although non-linearly) related to N and S , it can be assumed that for small variations of the carrier density ΔN the optical gain variation is proportional to ΔN , ΔS . This leads to $g = g_{th} + a\Delta N - a_p\Delta S$, using the local slopes $a = \partial g / \partial N$ (differential gain) and $a_p = \partial g / \partial S$. The approximation yields accurate results as long as $I_{pp} \ll I_{bias}$ for $I > I_{th}$, the small-signal regime conditions. Although such conditions are usually impractical in a communication setting, the small-signal analysis provides valuable insight into the characteristics of a DML. It can be shown that, under the small signal approximation and under sinusoidal excitation at angular frequency ω , the frequency response of the laser can be expressed according to:

$$H(\omega) = \frac{\omega_R^2}{\omega_R^2 - \omega^2 + j\omega\gamma}, \quad (6)$$

where f_R is the natural resonance frequency of the system, j is the imaginary unit and γ is the laser's damping factor. Assuming operation over threshold, f_R can be approximated as [22]:

$$f_R \approx \frac{1}{2\pi} \sqrt{\frac{v_g a \bar{S}}{\tau_p}} = \frac{1}{2\pi} \sqrt{\frac{\Gamma v_g a}{qV} \eta_i (I_{bias} - I_{th})}, \quad (7)$$

where \bar{S} denotes the average photon density. f_R is also called relaxation-oscillation or carrier-photon resonance frequency, as it determines the frequency of the transient damped oscillations

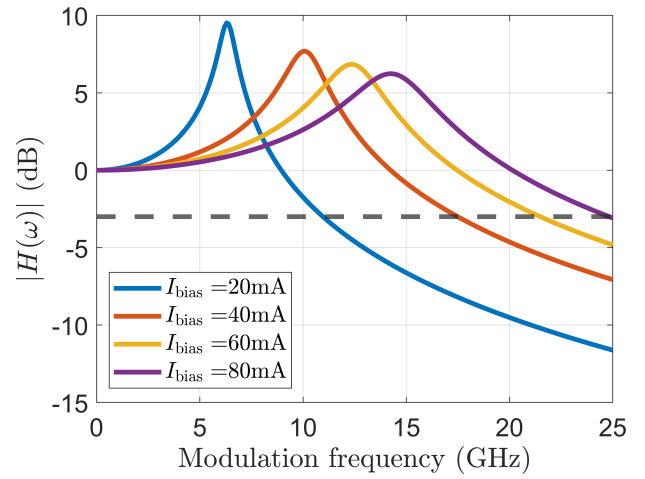


Fig. 2. Small-signal modulation response of a simulated DML. The dotted line shows the 3 dB bandwidth level

created in $S(t)$ and $N(t)$ due to the aforementioned carrier-photon interaction under current modulation. γ can be expressed as:

$$\gamma = Kf_R^2 + \gamma_0, \quad (8)$$

where K is the "K-factor" governing the laser response at high modulation frequencies and γ_0 is the damping offset. Both parameters are usually obtained through fitting from the modulation response curve (Eq. (6)).

The linear relation between ω_R^2 and $(I_{bias} - I_{th})$ describes the impact of I_{bias} in the modulation response of the laser. Such relation is shown in Fig. 2, where various frequency responses $|H(\omega)|$ are represented for different values of I_{bias} . It becomes apparent how the response shows a peak (that coincides approximately with f_R) and a rapid damping for frequencies beyond it. A 3-dB bandwidth f_{3dB} can be defined as the frequency for which the magnitude of the modulation response decreases to half of its DC value. For small γ , the approximation $f_{3dB} \approx 1.55f_R$ is often used. The small-signal intensity modulation (IM) of DMLs is therefore dictated by the I_{bias} level, with higher levels associated with a higher 3dB-bandwidth, although with diminishing returns due to the $(I_{bias} - I_{th})^{1/2}$ factor in Eq. (7).

B. Large-signal regime

The cost and power constraints in short-reach IM/DD systems favor amplifier-free operation. The large-signal regime describes the DML laser behaviour in most communication settings, where a high modulation index is desirable to overcome receiver noise while avoiding the use of amplifiers. This is due to the analytical solutions to the rate equations being unavailable in this regime (where I_{pp} and I_{bias} are comparable in magnitude). The most direct effect of a large I_{pp} is the introduction of signal intensity distortion due to the effect of relaxation oscillations. This effect is depicted in Fig. 3a, where overshoot and undershoot can be observed right after changes of the modulating current value. The larger instantaneous variation of N, S enhances the amplitude of the relaxation oscillations, introducing signal components uncorrelated to I . The instantaneous emission frequency ν can also show significant differences with respect to the small signal regime, as shown in Fig. 3b. The figure shows the variation of

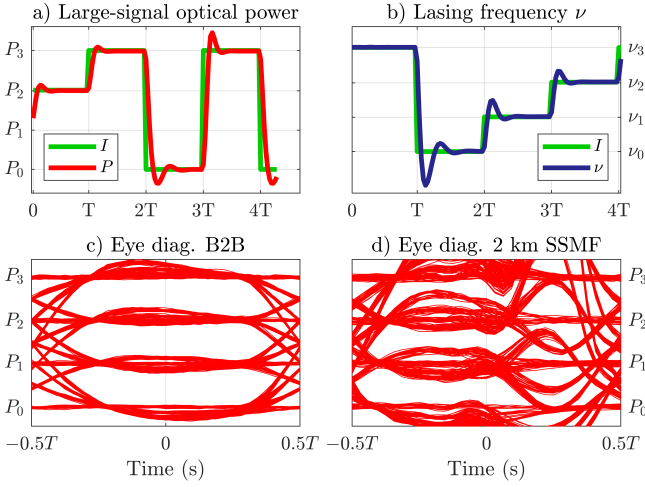


Fig. 3. Waveform distortion introduced by DMLs: a) relaxation oscillations, b) instantaneous chirp, c) simulated back-to-back eye diagram under 4PAM modulation and d) simulated eye diagram after 2km of SSMF, $R_s = 30$ Gbaud, central wavelength $\lambda = 1500$ nm. The power levels P_0, P_1, P_2, P_3 and instantaneous lasing frequency levels $\nu_0, \nu_1, \nu_2, \nu_3$ correspond to the 4 symbols in the 4PAM intensity modulation of I .

ν resulting from a current modulation. This is due to the signal chirp and relaxation oscillations resulting from the higher modulation index. Frequency chirping can induce a critical limitation of the transmission distance over a dispersive optical fiber. This is due to the interaction between chirp and CD in optical fiber, that induces pulse broadening on the envelope of the received optical signal. The effect of chromatic dispersion on a signal with nonlinear chirp is depicted in Fig. 3c, d, where the eye diagram of the simulated optical signal before and after transmission over 2 km of standard single-mode fiber (SSMF) is shown. The detrimental impact of pulse broadening is twofold: it decreases the peak optical power of the pulses while introducing ISI between neighboring symbols. It therefore entails substantial worsening of the effective SNR on top of the linear fiber-induced attenuation. The instantaneous chirp expression [23, 24] is obtained from the derivative of Eq. (3):

$$\Delta\nu = \frac{\alpha}{4\pi} \left[\frac{1}{P(t)} \frac{dP(t)}{dt} + \kappa P(t) \right], \quad (9)$$

and the factor κ is defined by:

$$\kappa = \frac{2\Gamma}{\eta h\nu_0 V} \epsilon, \quad (10)$$

where h is Planck's constant. The first factor in the sum of Eq. (9) is known as transient chirp, while the second is called adiabatic chirp. The prevalence of each chirp factor depends on the dynamics of P , and therefore on the variation of the input current I . The derivative term of the transient chirp makes it sensitive to fast variations of the optical power. This makes it especially prevalent in high R_s conditions, where the rapid variation of power makes its derivative large. The use of sharp pulses, like square pulses, induce high instantaneous derivative and high relaxation oscillation amplitude, leading to additional transient chirp in the output waveform. The adiabatic chirp becomes prevalent under high I_{bias} and optical output powers, especially at lower R_s . Chirp in DMLs is therefore unavoidable,

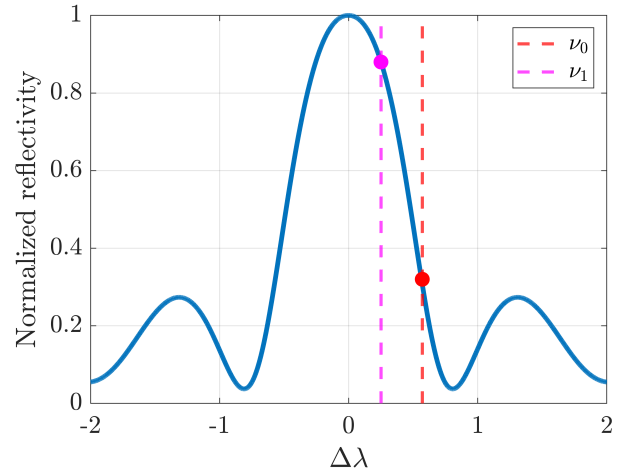


Fig. 4. Reflectivity vs detuning of a DBR. The modulation-induced chirp drives the lasing wavelength towards the maximum reflectivity peak

but the careful selection of certain configuration parameters ($I_{\text{pp}}, I_{\text{bias}}$, pulse shape) could help mitigate it.

The limited modulation bandwidth of DMLs is associated with several factors, including the aforementioned carrier-photon interaction. Such factors introduce linear and nonlinear memory effects, that become apparent as R_s increases. Although Eq. (6) gives meaningful insight on the characteristics of the DML, the DML response depends on the laser configuration, including $I_{\text{bias}}, I_{\text{pp}}$, and pulse shaping, and can only be obtained through numerical simulations. Additionally, the susceptibility of the system to timing and amplitude impairments varies depending on the channel characteristics. Thus, the use of eye diagrams (Fig. 3c and d) is widely used in the evaluation of experimental DML-based systems in the large signal regime, as it allows to qualitatively assess the signal degradation at the receiver.

C. Coupled-cavity effects

Through the use of additional passive and active laser sections in the laser structure, it is possible to overcome the physical limitations that hinder the DML modulation bandwidth beyond 40 GHz [22, 25–28]. Among the various techniques used, detuned loading and photon-photon resonance (PPR) have delivered promising results in several implementations. Detuned loading is based on the combined effect of distributed reflectors, mostly distributed Bragg reflectors (DBRs) and modulation-induced chirping in order to enhance the dynamic response of the DML [29, 30]. This is achieved through the design of the gain and reflective sections, so the range of main lasing wavelengths is detuned from the main lobe of the DBR reflectivity spectrum. Fig. 4 shows the instantaneous lasing frequencies ν_0, ν_1 , associated with 2 different pump current levels I_0, I_1 . Both frequencies fall on significantly different regions of the DBR reflectivity spectrum, leading to a difference in mirror loss and the effective differential gain a_{eff} . The approximation of f_R in Eq. (7) must therefore be modified to account for the detuning $\Delta\lambda$ from the DBR central wavelength:

$$f_{R,DL} \approx \frac{1}{2\pi} \sqrt{\frac{v_g S}{\tau_p} \Re [\tilde{\Gamma}_z(\Delta\lambda) g_0 (1 + j\alpha)]}, \quad (11)$$

where $\tilde{\Gamma}_z(\Delta\lambda)$ is the complex reactive confinement factor in the active section [30]. The larger the imaginary part of this factor becomes, the larger the impact of α (proportional to chirp) becomes, enhancing f_R . When $\Delta\lambda = 0$, $\tilde{\Gamma}_z(\Delta\lambda)$ becomes real, and therefore no f_R advantage is obtained from the passive section. Detuned loading is therefore an effective method to exploit the FM derived from direct modulation by enhancing the IM, resulting in higher modulation bandwidth. This is not only desirable from the IM bandwidth perspective, but it can also mitigate chirp, leading to reduced distortion after fiber transmission [31].

PPR bandwidth enhancement is based on the interaction between longitudinal modes in the laser cavity. When such modes are close in wavelength, they can still be coupled, [32, 33] leading to a potentially faster modulation response compared to the single-mode configuration. This is usually done through amplification of a secondary side mode using a coupled reflective cavity, as in the case of detuned loading. Both approaches are mutually compatible, resulting in further enhancements in modulation bandwidth. In the case of PPR, a key design goal is to tune the grating phase to match the round-trip phase of the main mode and the side mode, forcing constructive interference between themselves. In this fashion, Γ shows also a time dependency, due to the time-varying interaction between the modes in the cavity. The combined gain of the two modes makes possible to force a second resonance peak, of higher frequency than the carrier-photon resonance, to appear in the modulation response of the DML.

D. High-speed DMLs

The modulation performance of DMLs, based on both in-plane lasers [2, 26, 34–37] and vertical cavity surface-emitting lasers (VCSELs) [38–42] structures, has been extensively developed through cavity design. It must be noted that the commercial interest of DMLs often resides in their energy efficiency and cost, and considerations like reliability, output power and thermal performance play a role in their development. Their comparison must therefore go beyond modulation bandwidth, and a more holistic assessment must be made [2]. Within the cavity design choice, several structures and substrates have been employed in the development of high-bandwidth (f_{3dB}) DML lasers. >50 GHz bandwidth was achieved in [43] using push-pull modulation, where the current is injected on two locations within the cavity. The driving of the laser is designed so an increase in one of the currents leads to a decrease in the other, and viceversa. Through the combined use of a MQW active region and a single DBR section enhancing detuned loading and PPR, uncooled >100 GHz bandwidth was obtained in [8], maintaining >70GHz at 85°C. The combination of detuned loading and PPR has been used in several works, obtaining f_{3dB} between 40 and 65GHz [1, 6, 7, 44]. As a general overview, several configurations have achieved bandwidths over 50GHz, but 100 GHz have been reached using more complex and costly fabrication processes [2].

3. SYSTEM MODELING

Modeling a dynamic system is a fundamental first step to its optimization. In the case of DMLs, several alternatives are available depending on the computational resources available, time constraints and desired accuracy and exhaustiveness of the modeling. In this section we introduce some of the most common approaches, sorting them from the more physics-intensive ones to the purely data-driven.

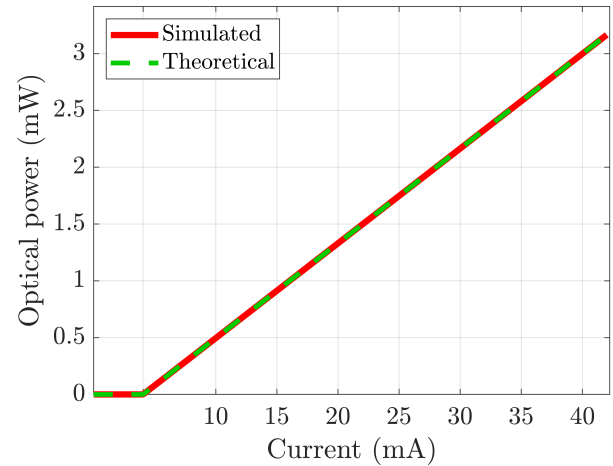


Fig. 5. P-I curve associated with the simulated DML. Depending on the physical structure of the laser and thermal effects, the power response of the laser might show nonlinearities

A. Parameter extraction and ODE solvers

Given that the previously introduced rate equations (Eq. (1)–(3)) yield accurate prediction of the DML response in line with experimental verification [45–47], they may seem as the most direct way of estimating the system response. However, they entail 3 main challenges:

- Most of their parameters are not easily measurable
- They require the use of numerical ordinary differential equation (ODE) solvers in the large signal regime
- Analytical gradients are unavailable due to the computational structure of ODE solvers

The problem of parameter extraction has been extensively treated in the literature [45–48]. Iterative techniques allow to obtain all the relevant parameters based on experimentally obtained data, like the lasing spectrum, the modulation response (Fig. 2), the static light-current (L-I) curve (Fig. 5) or the spontaneous emission spectrum of the laser. Through the use of machine learning, it is possible to automatize this process, simply by providing the algorithm with the necessary figures of merit, avoiding manual calculation of parameters [49]. Yet, quantities like N_0 are not directly measurable, and must be estimated through related parameters, leading to potential inaccuracy.

Even when all the necessary parameters are available, the use of ODE solvers may prove impractical in some scenarios. The large values of S and N can lead to instability in the numerical calculation, leading to divergence and failure of the method. This makes convergence analysis a must have when using ODE solvers, and re-initialization of the calculation may be needed [50]. The sequential nature of the widely used Euler-based methods [51] makes parallelization challenging, leading to computational bottlenecks depending on the analyzed system. The largest advantage of such methods is their configurable precision, but the computational toll associated with high precision must also be considered. Lastly, ODE solvers make use of local gradient approximations in order to solve differential equations. This collides with the concept of automatic differentiation that many machine learning and optimization frameworks use,

where systems are usually built on functions with known analytical derivatives [52, 53], making gradient calculations faster. This drawback makes an automatically differentiable model of DMLs desirable, as it may allow the simultaneous optimization of large parameter spaces in a relatively reduced computation time. The next subsections will describe some of the available alternatives for the modeling of DMLs.

B. Circuit-equivalent models

Circuit-equivalent models [50, 54–59] represent a less complex alternative to rate equation solvers, while sharing the interpretability of physics-based models. They make use of electrical components (amplifiers, capacitors, resistors...) to model the dynamic behaviour of the laser by relating their characteristics to the laser's rate equation parameters. Thus, they are able to reproduce the behaviour of a wide variety of lasers, as long as the corresponding parameters can be measured. The use of current and voltage signals as sole dynamic variables makes them an ideal candidate for circuit simulators, thus facilitating the task of building a numerical simulation. Some literature has included the Langevin phase and intensity noise sources in the simulation, [60, 61] thus introducing significant acceleration with respect to noisy rate equations, where stochastic local gradients can worsen the performance of adaptive step solvers.

On the other hand, circuit-based models share some of the pitfalls of ODE solvers. Firstly, although circuit simulators are optimized for the task, exhaustive models can be relatively complex, introducing significant computational burden to the simulation [59]. This becomes especially true in optimization scenarios, where circuit-specialized software cannot be utilized, and the numerous differential relations between variables must be obtained numerically, i.e. with ODE solvers. In conclusion, although they can be useful in the design and simulation of DMLs, circuit-equivalent models are so far impractical as part of a gradient-based optimization pipeline, and automatically differentiable alternatives should be developed for this purpose [12].

C. Interpretable data-driven modeling

The mathematical modeling of dynamic systems (based on underlying physics, data, or a mixture of both) has been studied extensively in the control theory community, in what is usually called system identification [62, 63]. A fundamental advantage of data-driven modeling is its compatibility with numerical optimization techniques: they are mostly based on continuous, easily differentiable functions that provide numerical stability in the search of optimal configurations. Some of the most popular approaches for discrete linear systems are variations of autoregressive such as integrated moving average models (ARIMA) [64–66]. These models combine the use of 3 techniques: the evaluation of past outputs to predict future ones (AR), the discrete differentiation of the time series in order to force its stationarity (I) and a moving average (MA) of the past prediction errors. However, due to the nonlinear nature of the DML behaviour, many classical system identification models cannot be applied. Additionally, ARIMA models are based on endogenous time series, i.e. the sequence they make predictions on is determined solely by its past values. In order to model nonlinear dynamics, higher-order temporal dependencies and/or nonlinear activations are often used. Nonlinear autoregressive exogenous models (NARX) [67, 68] are a common choice in this case, as they combine linear operations with a static nonlinearity that allows to model a larger function space. Defining an input $u(n)$, an

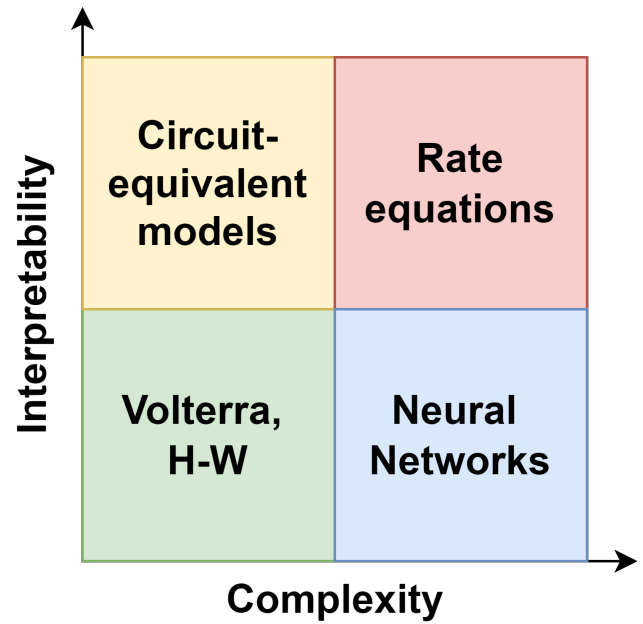


Fig. 6. Relation between complexity and interpretability of the proposed modeling techniques

estimated output $\hat{y}(n)$, a input feature vector $x(n)$, a learnable parameter space θ , a and a static nonlinear function h , a generic NARX model expression can be obtained:

$$x(n) = [\hat{y}(n-1), \dots, \hat{y}(n-N_y), u(n), \dots, u(n-N_u)], \quad (12)$$

$$\hat{y}(n, \theta) = h(x(n), \theta), \quad (13)$$

where N_u, N_y are the input and output memory length, respectively. This general definition includes a large variety of functions, with different nonlinearities, recursivity schemes and complexity levels.

Volterra filters are often used in communication-oriented DSP to model and/or compensate for the dynamics of nonlinear system [69–72]. They are among the simplest NARX models, as they do not employ recursion, and nonlinearity is achieved through multiplication of past input samples with each other. They are based on Volterra series [73], a variation of the Taylor series where instead of evaluating the analyzed function around a single point, it is evaluated over an infinite range of past samples. Given the previous definitions of $\hat{y}(n), u(n)$ the discrete-time Volterra series can be evaluated as:

$$\begin{aligned} \hat{y}(n) = & h_0 + \sum_{k_1=0}^{\infty} h_1(k_1)u(n-k_1) + \\ & \sum_{k_1=0}^{\infty} \sum_{k_2=0}^{\infty} h_2(k_1, k_2)u(n-k_1)u(n-k_2) + \dots \end{aligned} \quad (14)$$

where h_0, h_1, \dots, h_n are the Volterra kernels and k_1, k_2, \dots, k_n are the delays associated with every kernel order $1, 2, \dots, n$. As in the case of the Taylor series, increasing the order of the series delivers potentially higher accuracy in the representation, at the cost of increasing complexity [74, 75]. This forces real implementations to truncate the Volterra series in both kernel order and delay, leading to Volterra filters. It must be noted that the Volterra filter of order 1 corresponds to the linear convolution

operator, and therefore the Volterra kernels can be interpreted as a higher-order impulse response of the analyzed system. Fig. 6 shows a comparison in terms of interpretability and potential complexity between data-driven and physics-driven modeling methods. The main challenge when using Volterra filters is the calculation of optimal kernels. There are several techniques developed for this purpose [76–78], but numerical multivariate optimization techniques can also be used at the expense of higher computation time.

Hammerstein-Wiener (H-W) models [67] are an alternative to NARX-based system identification, and provide design flexibility while including a larger number of hyperparameters to be tuned. They are based on the combination of an input static nonlinear function h , a linear infinite impulse response (IRR) filter $z(n)$ defined by the real or complex coefficients p_i, q_i and an output static nonlinear function g . Its mathematical expression is:

$$w(n) = h[u(n)] , \quad (15)$$

$$z(n) = \sum_{i=1}^{N_z} q_i z(n-i) + \sum_{j=0}^{N_w} p_j w(m-j) , \quad (16)$$

$$\hat{y}(n) = g[z(w(n))] , \quad (17)$$

where N_w, N_z are the number of input and output delays, respectively. The choice of h, g and the delay orders N_w, N_z must be tailored to the specific system to be modeled. Although the nonlinearity choice is usually hyperparameter-optimized among a pool of usual functions (sigmoidal, piece-wise continuous, wavelet), the linear transfer functions can be estimated through gray-box modeling (combination of a-priori physical knowledge with data-driven approaches), numerical optimization or stochastic models like the expectation-maximization (EM) algorithm can also be used [79]. One of the main advantages of H-W models resides in their interpretability, given that the linear transfer function governing them can be analyzed with traditional spectral analysis as any other linear filter (Laplace/Z transforms, etc). When the physics of the nonlinear system to be modeled are unknown or too complex to be represented in such structure, purely data-based approaches, like neural networks (NNs), are a popular approach [63].

D. Neural networks

NNs are mathematical structures where complex calculations would be performed through the combination of large numbers of simpler operations [17]. Their potential resides in the use of relatively simple linear functions followed by a nonlinear activation. Although, as in the case of Volterra filters, they can be considered a NARX model, their advantage resides in their structural flexibility, that allows them to specialize depending on the task to be performed. The concatenation of simple mathematical operations within NNs leads to large, usually non-orthogonal parameter spaces. Such spaces must be optimized to meet a certain objective, abstracted into a loss or cost function. This is usually done through gradient-based numerical optimization techniques, where instead of calculating the overall function gradient analytically, it is approximated based on reduced subsets of the training data (mini-batches). This procedure accelerates the overall gradient calculation, leading to high performance models without explicit physical knowledge of the system under investigation. The main inconvenient of this procedure is

however their lack of interpretability: the concatenation of nonlinearities within NNs them makes it difficult to understand the interaction between the different parameters in the network.

NNs have been widely used in the modeling of optical communication systems and subsystems [80–83]. Many of the NN architectures in the field have tried to embed some temporal context into the network, as many of the systems found in communications have memory elements. Time-delay neural networks (TDNNs) [84, 85] are a special case of feedforward neural networks (FFNNs), where no recursive element is added to network. Instead, the input of the network is built as a sliding window of past samples, thus providing the network with temporal context while maintaining relatively low complexity. Single-dimensional convolutional neural networks (CNNs) [86] work on the same principle as TDNNs, although they sometimes inherit pooling layers from its higher-dimensional counterparts. Another possible approach to address this problem is using recurrent neural networks (RNNs), where the network output depends not only on the input features, but also on the state tensor in each neuron. This tensor gives the network encoded temporal context on the past inputs and outputs of the model, leading to potentially better prediction of models with temporal dependencies. Gated recurrent units (GRUs) [87] and long-short term memory (LSTM) [88] are two of the main architectures in this paradigm. One major limitation of such networks is the modeling of long temporal dependencies, due to the exploding and vanishing gradient problem [89]. The transformer architecture has been extensively used due to its success overcoming these problems in the natural language processing community [90]. This has encouraged its use in the modeling of optic-fiber channels [91, 92]. Our work in [10] demonstrated the use of a variation of the transformer architecture, the convolutional attention transformer (CAT) [11] in the modeling of DMLs. Based on the structural similarities between neural ODEs and the residual connections in transformers [93], we use the outputs of the DML rate equations to obtain a differentiable DML model. The model compared favourably to hyperparameter-optimized Volterra filters, TDNNs and LSTMs [10].

4. END-TO-END OPTIMIZATION

The throughput limitations of DMLs have also been studied from the DSP perspective. In this scope, we can distinguish 2 different trends: one of them aims to exploit the available bandwidth to increase spectral efficiency, while the other aims to compensate the DML-induced waveform distortion. Discrete multi-tone (DMT) [94], probabilistic constellation shaping (PCS) [95] and GCS are the dominant technologies in the former category. DMT (the baseband, guided-system equivalent of orthogonal frequency-division multiplexing, OFDM) aims to exploit the available bandwidth through the use of multiple digital narrow-band sub-carriers, instead of using a unique one spanning all the available spectrum. In non-flat spectrum conditions, like the induced by PPR in DMLs, the SNR varies along different regions of the spectrum. The use of DMT allows higher granularity on the configuration for each sub-channel, optimizing it to the local conditions of each narrow band. PCS aims to replace uniform probability mass function (PMF) of the transmitted symbols by a different PMF in order to optimize a certain metric (energy per bit, SNR). GCS [20] follows similar approach, but it modifies the energy allocated to each symbol instead of tweaking their probabilities. The combination of DMT and constellation shaping is usually called entropy loading [96], and it allows to adapt

the symbol distribution to the spectral channel response, saving power in the high-SNR narrow bands while maximizing it in the low-SNR bands. Many DML implementations have included a combinations of these technologies to increase the throughput of DMLs [28, 97–99]. Pulse shaping is another source of throughput optimization. Faster-than-Nyquist (FTN) [100] signaling aims to exploit this by introducing a controlled amount of ISI in each symbol, correcting their introduced correlation on the RX side. This allows to increase the effective throughput, as long as the receiver is able to compensate both the TX- and the channel-induced ISI. [28] combines FTN with entropy loading for increased spectral density of the DML bandwidth. Within distortion compensation schemes, most approaches are focused on either tailoring the peak-to-peak current to invert the non-linear DML response or using pre-distortion and equalization techniques. [101] provides a linearization method to correct the DML nonlinearities, while [102] aims to suppress relaxation-oscillations using ML approaches. Even optical filters can be designed through semi-analytical approaches to find optimal cavity configurations [4]. The development of DML-specific compensation approaches is also extensive, using different equalizer structures like Volterra [103, 104], TDNN [9], RNN [105] or deep belief networks [106].

Despite the remarkable performance leap obtained in some of the aforementioned data-driven approaches, their optimization is based on single-sided or sequential learning approaches: they do not optimize the TX and RX sides jointly. In sequential learning, each side of the communication link (TX and RX) is optimized keeping the configuration of the other one fixed, thus avoiding the need for gradient propagation across the transmission channel. E2E learning [16] aims to condense several functions within TX (constellation shaping, pulse shaping, bit labelling) and RX (EQ, symbol decoding) into a single neural network, where the link configuration is optimized simultaneously at both ends based on a certain metric (loss function). Thus, the performance of the configuration obtained through E2E learning is limited mainly by the amount of DSP functions optimized and the accuracy of the modeling of the elements between TX and RX. This can pose a considerable challenge in the case of DML-based systems, where the building a differentiable model of the DML is not straightforward, as discussed in the previous section. Gradient-free approaches, based on derivative-free optimizers or reinforcement learning, have been proposed in the training of E2E [14, 21, 107]. Nonetheless, they introduce severe computational overhead and their gradient approximations can lead to numerical optimization issues [15]. Several gradient-based have been proposed for DML (VCSEL) systems, implementing GCS [108] and pre-distortion + EQ [109] based on data-driven DML models. The present work aims to jointly optimize transmitter GCS and LPS and receiver EQ with the driving configuration of the DML (I_{bias} , I_{pp}), thus tailoring E2E learning to the specific characteristics of DML-based systems. This entails extending our DML modeling work in [10], obtaining a model that is able to predict the dynamics of the laser regardless of its biasing.

The usual approach to E2E learning in communication systems is using autoencoders (AEs) [17] as substitutes of the DSP pipeline [16, 110, 111]. This is due to their functional resemblance to a communication link: they compress information subject to physical constraints (encoding) to then retrieve it with the minimum loss of information possible (decoding). The AE was created to compress and decompress information with minimal information loss, making it an ideal candidate for this task. It consists on an encoder, that performs the dimensionality re-

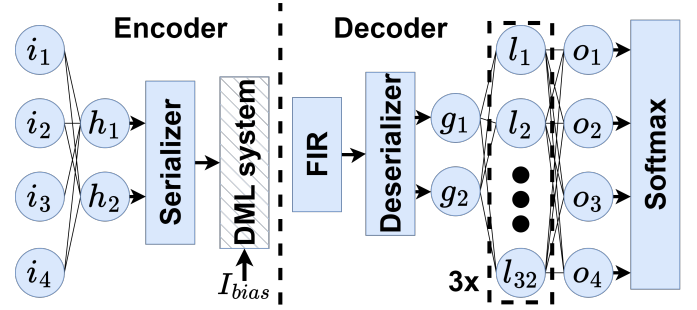


Fig. 7. Architecture of the proposed AE

duction, and a decoder, that aims to retrieve the information compressed by the encoder (as shown in Fig. 7). AE-based optimization of communication systems [21, 110] usually relies on an encoder to map an alphabet of one-hot encoded symbols i_n to a vector of samples h_n representing a symbol (assuming 2 sps in Fig. 7) to be transmitted. The decoder then maps the received samples g_n back to scalars o_n representing output probabilities, usually after a series of hidden layers, represented by l_n in Fig. 7. It must be noted that the matrix multiplication in AEs introduces a significant complexity overhead to the TX and RX operation. Therefore, AEs are often used only to find optimal link configurations, that are then implemented in the form of less complex look-up tables and decision circuits. This allows to take advantage of the performance gains yielded by autoencoders while adjusting complexity to the requirements of optical transceivers [112]. The standard AE [17] is an FFNN, and therefore it lacks any memory mechanism in its structure. This explains the use of a finite impulse response (FIR) filter on the decoder side, that allows the AE to capture and compensate for ISI and undesired memory effects. The o_n are then masked with a normalized exponential function (softmax), depicted in Eq. (18).

$$\sigma(o_n) = \frac{e^{o_n}}{\sum_{j=1}^N e^{o_j}} \quad (18)$$

where N is the number of neurons in the decoder output layer. The softmax function converts the single-dimensional output tensor in an array of normalized probabilities, thus giving insight on the certainty of the symbol prediction. As in any supervised learning scheme, the AE needs to be trained based on a certain loss function. Given that the goal of the link optimization is minimizing the loss of information over the transmission channel, a metric that captures this information loss is desirable. This leads to the use of categorical cross-entropy (CE) as an indirect estimator of mutual information between transmitted and received symbols [21]. The expression of CE is shown in Eq. (19):

$$J_{CE}(\theta) = \frac{1}{N} \sum_{n=1}^N \left[- \sum_{m=1}^M i_m^{(n)} \log o_m^{(n)}(\theta) \right], \quad (19)$$

where N represents the symbol batch size and M represents the modulation order utilized. In the backpropagation stage of the training process, the gradient over trainable parameters θ is calculated to minimize CE. This leads to higher mutual information between both ends of the link, due to the approximation of its lower bound in Eq. (20):

$$I(X;Y) \geq H(X) - \hat{H}(X|Y), \quad (20)$$

Parameter	Symbol	Value	Units
Confinement factor	Γ	0.24	-
Photon lifetime	τ_p	2.60	ps
Carrier lifetime	τ_c	3.17	ns
Transparent carr. dens.	N_0	$2.00 \cdot 10^{24}$	m^{-3}
Active cross section	σ_g	$3.34 \cdot 10^{-20}$	m^2
Eff. refractive index	n_g	4	-
Active volume	V	$3.60 \cdot 10^{-17}$	m^3
Gain compression	ϵ	$2.00 \cdot 10^{23}$	m^3
Spont. emiss. factor	β	$1.00 \cdot 10^{-3}$	-
Diff. quant. eff.	η_0	0.20	-

Table 1. Utilized parameters for the rate equation laser simulation

where $H(X)$ is the entropy of the probability distribution of the transmitted symbols X and $\hat{H}(X|Y)$ is the upper bound on the conditional entropy of X given the probability distribution of the received symbols Y . $\hat{H}(X|Y)$ can be approximated by the CE between transmitted and received symbols, given that the expression of the true channel transition is unknown [21].

5. SIMULATION SETUP

The proposed DML system optimization is based on two main components: the laser surrogate model and the E2E optimization approach. The surrogate model aims solely to reproduce the laser behaviour as accurately as possible. The E2E approach finds the optimal system configurations subject to the constraints imposed by the surrogate model dynamics and its loss function, once the surrogate model has been trained.

A. Surrogate model

The structure of the surrogate CAT model, depicted in Fig. 9, is based on 3 building blocks: learned positional embeddings, convolutional attention and dense layers with ReLU activation. The positional embeddings aim to capture the position of each sample within the sequence, giving temporal context to the network. The convolutional attention block aims to discern the most relevant input samples for the calculation of each output sample through the use of matrix multiplication and learned convolutional filters. Lastly, the dense layers provide depth to the network, as they contain most of the trainable parameters within it. Although the model architecture, shown in Fig. 9, is identical to [10], in this work we introduce a new data generation process. This allows to maintain model complexity with respect to our previous work while achieving a DML model agnostic to the waveform shape, the bias, and the peak-to-peak amplitude of the input sequence.

The surrogate modeling is performed in a data-driven fashion, using the laser rate equations (Eq. (1)–(3)) as source of data. The dataset of input waveforms to the rate equations is obtained by generating 4PAM-modulated symbols, pulse shaped at 2 samples per symbol (sps). The rate equation parameters utilized are specified in Table 1. The utilized parameters correspond to a generic DFB laser with $f_R = 10.6$ GHz and a f_{3dB} of 25.5 GHz at $I_{bias} = 75$ mA. Although the parameters are not chosen to match

the specifications of a real device, they are of the same order of magnitude as those reported in the literature for single-mode quantum-well DFB lasers [113, 114]. It must be noted that $\phi(t)$ is not considered, given that the simulated setup is back-to-back. Therefore the values of α and κ do not have an impact in the behaviour of the surrogate model. The region of the modulation response beyond f_R is of special interest due to the increased data throughput and significant waveform distortion introduced. The CAT model was therefore trained separately on 3 relatively high R_s , namely {15, 20, 25} Gbaud.

The generalizability in terms of waveform shaping is addressed by using 2 different types of pulse: square and stochastic pulses. The steep slope of the square pulse-shaped symbols allows to capture the transient dynamics of the DML response, while the stochastic pulses are used to prevent overfitting. The stochastic pulses are implemented through a 2-tap finite impulse response (FIR) filter, where the filter coefficients are drawn from a uniform distribution in the interval $[-0.5, 0.5]$. The pulses are normalized in amplitude to avoid distorting the 4PAM symbols. In order to maintain a high modelling accuracy regardless of the combination of I_{bias} and I_{pp} utilized, both quantities are randomized for the generation of the input waveform data set. This is achieved by randomizing I_{bias} , drawing it from a uniform distribution in the interval $I_{bias} = [50, 100]$ mA. I_{pp} is randomized in a similar fashion but constrained to the range $I_{pp} = [0, 80]$ mA, in order to maintain a driving current significantly higher than the threshold current $I_{th} = 4.06$ mA for all I_{bias} and I_{pp} combinations. This will allow the optimization of the E2E learning approaches in a wide variety of different input currents, allowing the use of I_{bias} and I_{pp} as trainable parameters.

Once the driving waveforms are generated, the sequences are then oversampled to 32 sps and low-pass filtered (LPF) to constrain their bandwidth to $0.9R_s$. This is done to ensure the accuracy and convergence of the numerical solution to the rate equations, even if the surrogate model will operate on a 2-sps basis. The target (ground truth) output sequences for the CAT surrogate models are obtained by inputting the previously described driving waveforms to a numerical solver of the laser rate equations at a certain (randomized) I_{bias} . The output photon density sequences from the rate equations are then down-sampled and converted to optical power waveforms through Eq. (4). The loss function of the model is defined comparing the sequences from the rate equation solver to the predictions of the surrogate model using normalized root mean squared error (NRMSE). The use of NRMSE provides better loss interpretability, as the normalization applied makes the calculation of the loss relative to the amplitude of each generated sequence. Once the surrogate model is trained, its weights are fixed and it is used as part of an E2E optimization approach.

B. E2E approach

The E2E optimization approach aims to find the optimal combination of TX, RX and laser-driving parameters in order to minimize the probability of decision errors after detection. The approach should therefore reach optimal performance regardless of the targeted laser cavity structure, as long as the surrogate DML model is able to reproduce the laser behavior accurately. Thus, our approach paves the way for the E2E optimization of optical communication system based on external modulators, like electro-absorption modulators (EAMs), as long as data availability allows for the training of a sufficiently accurate surrogate model. The investigated back-to-back IM/DD system is represented in Fig. 8. The modulation is based on equiprobable 4PAM

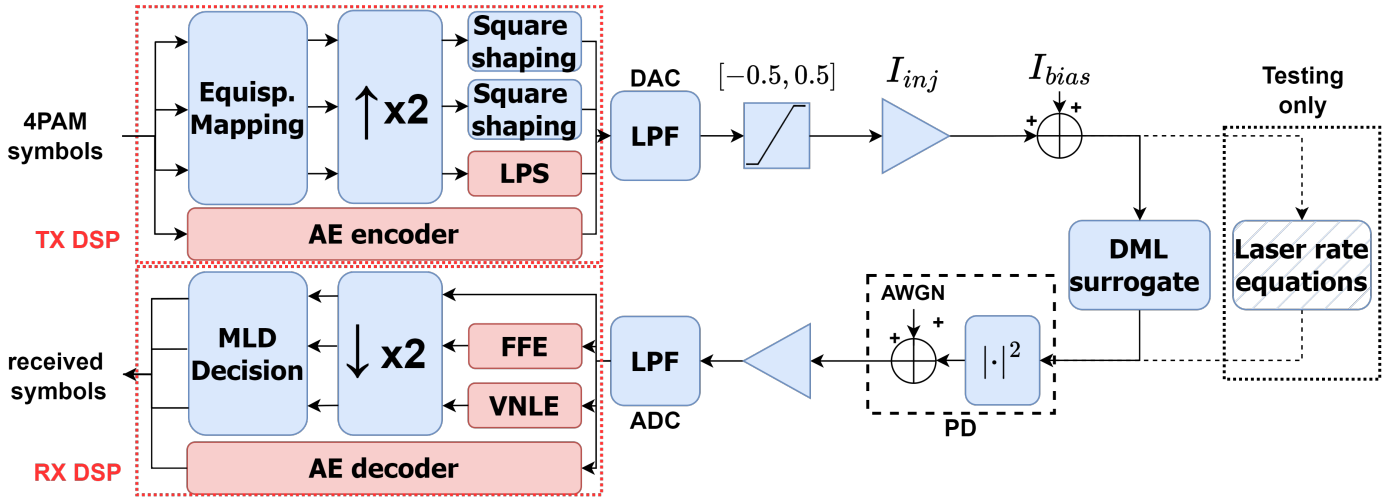


Fig. 8. Block diagram of the proposed DML optimization approach. The trainable blocks are highlighted in red

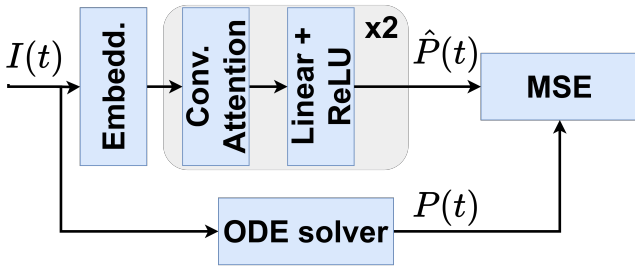


Fig. 9. Architecture of the CAT. The network sub-blocks are described in Section 5

	BL/FFE	VNLE	AE
I_{bias} (mA)	75	75	Learnable
I_{pp} (mA)	[8, 80]	[8, 80]	Learnable
Pulse shap.	Square	Learnable	Learnable
GCS	Equispaced	Equispaced	Learnable
Filt. taps	0/21	272	11
DML model	Rate eqs.	CAT	CAT
Loss	MSE	MSE	CE

Table 2. Parameters of the compensation approaches

symbols, upsampled to 2 sps. The TX establishes the GCS constellation intensity levels and the 2-tap pulse shaping in order to generate the modulation current sequences. The hardware limitations of the digital-to-analog and analog-to-digital converters (DAC/ADC) are modeled as FIR LPFs, with a bandwidth $B_{LPF} = 0.9 \cdot R_s$. The impact of impairments associated with DAC and ADC is not considered in this paper. However, the AE is trained to take into account the limited time resolution and BW of DAC and ADC. After filtering, the sequences are constrained to the range $[-0.5, 0.5]$ and then amplified to $[-40, 40]$ mA for a maximum peak-to-peak I_{pp} of 80 mA, in order to match the surrogate data generation. I_{bias} is again constrained to the range $[50, 100]$ mA. During training, the emulation of the DML

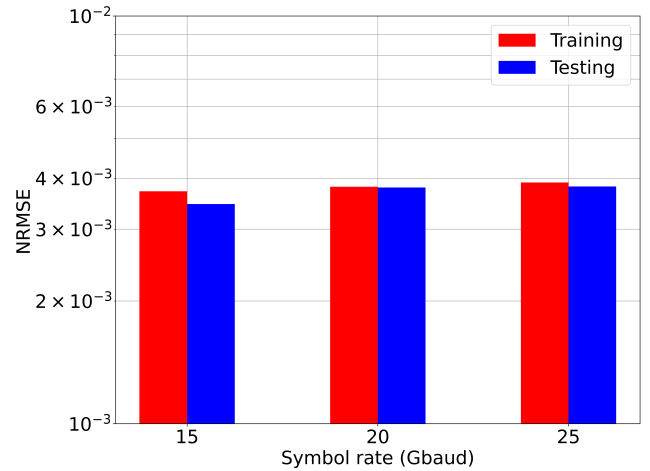


Fig. 10. Training and testing NRMSE scores of the CAT surrogate, using the laser rate equations as ground truth

response is carried out by the surrogate model, as its architecture allows for automatic differentiation. The testing is however conducted on the laser rate equations, using the same parameters as for data generation. This allows to obtain more reliable performance metrics, as the surrogate may distort them due to modeling inaccuracies.

After generating the output sequences from the DML models, additive white Gaussian noise (AWGN) samples are added to the signal after square-law detection. The noise variance is fixed to yield 22 dB electrical signal-to-noise ratio (SNR) at the highest average P_{rec} (corresponding to $I_{pp} = 80$ mA). The value of I_{bias} does not impact P_{rec} , as only the peak-to-peak power is considered in it. Lastly, the adaptive RX DSP performs 2-sps-wise EQ, downsampling and symbol decision. The SER and MI performance metrics are obtained by comparing the estimated symbol probabilities at RX with the originally sent sequence at TX, using maximum likelihood detection (MLD) or softmax activation depending on the approach. The compensation of the system is based on four different approaches: the baseline uncompensated system (BL), an RX-side FIR FFE, a second-order VNLE with a

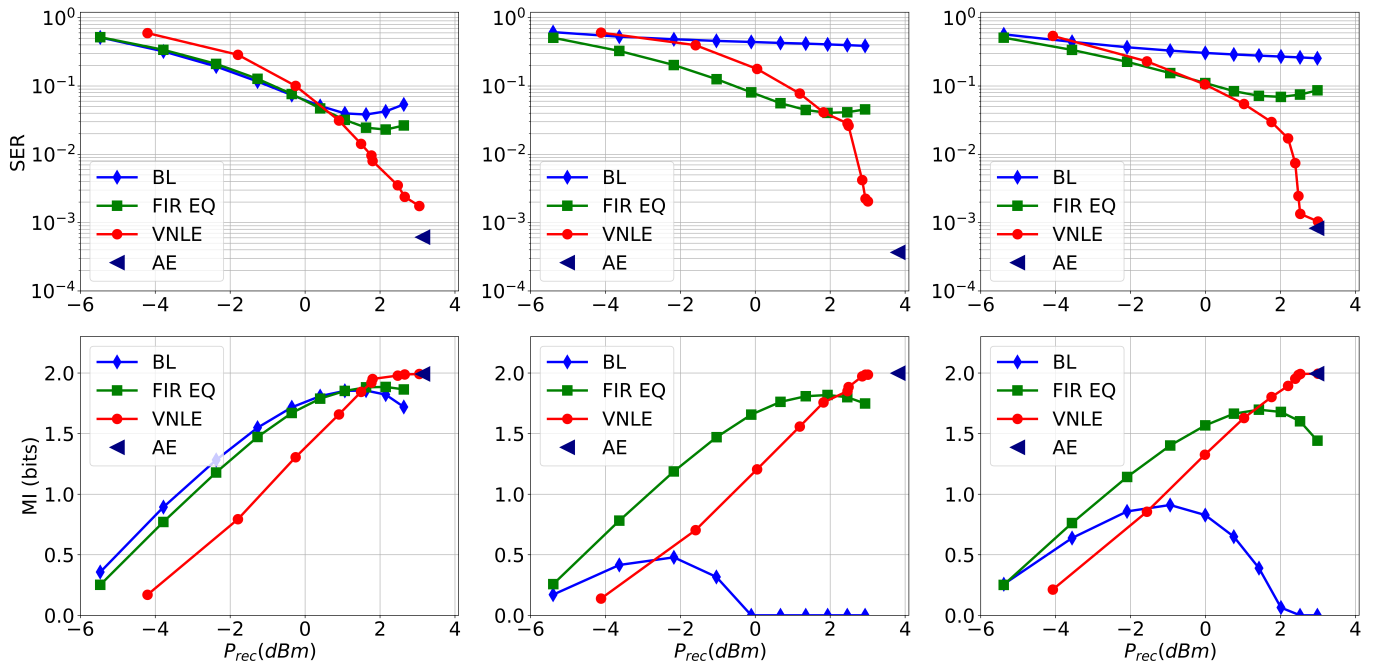


Fig. 11. Symbol error rate (SER, top) and mutual information (MI, bottom) results at symbol rates $R_s = \{15, 20, 25\}$ Gbaud (left, middle, right) for the uncompensated baseline (BL), finite impulse response equalizer (FIR EQ), Volterra nonlinear equalizer (VNLE) and autoencoder (AE) setups

transmitter LPS and an AE. Table 2 lists the specific parameters for each approach. The FFE is meant to emulate the conventional approach to DML-based system optimization, while the VNLE and AE give insight on the performance advantage of E2E models. It must be noted that only the AE handles I_{pp} and I_{bias} as trainable parameters, while all the other models are kept at fixed bias and swept through various I_{pp} (and therefore P_{rec}) values. Fig. 7 shows the encoder and decoder AE architecture from input symbol i_n to output symbol likelihoods o_n . The encoder, or TX side, is based on a single linear layer to map the input one-hot encoded vectors into 2-sample pulses. All the obtained pulses are then serialized into 1024-sample time sequences to be used as driving current to the DML. The I_{bias} level is added to the signal after filtering and amplification, as explained previously. On the decoder (RX) side, the received sequences are first FIR filtered in order to provide a memory mechanism to the AE. After deserialization, 3 leaky-ReLU-activated feedforward layers with softmax activation at the output convert the filtered samples into symbol probabilities for decision. The AE loss is then calculated using cross-entropy (CE) between the originally transmitted symbols and their assigned symbol probability at the receiver.

6. RESULTS

A. Surrogate model

The surrogate model training comprises 2^{23} samples in sequences of 1024 samples, while the testing data set includes 2^{17} samples. The randomization of pulse shape and laser driving configurations is performed on a per-sequence basis. The training and testing NRMSE scores obtained by the CAT model are depicted in Fig. 10. Throughout the three analyzed R_s , the testing NRMSE loss is slightly lower than its training counterpart,

giving no sign of overfitting. Another interesting trend is the slight increase in NRMSE as R_s increases. This trend might be related to the predominance of the nonlinear effects at higher R_s , leading to potentially more complex DML dynamics. In any case, the three models perform well below the 1% mark.

B. E2E approach

The symbol dataset of the E2E approaches comprises 2^{20} symbols, with an 80/20 partition between training and validation, respectively. The dataset is split in mini-batches of 512 symbols for exploiting parallelization to reduce the training time. The I_{pp} to all the models except the AE is swept in the range $[8, 80]$ with a step of 8 mA between consecutive levels.

Even though all the approaches are subject to the same I_{pp} constraints, the E2E approaches are able to exploit the DML transient response through LPS (and GCS in the case of the AE), yielding higher P_{rec} . The AE is able to optimize its I_{pp} dynamically within the constrained range, therefore only one AE power level was analyzed. The training is iterated over three different symbol rates: 15, 20 and 25 Gbaud, matching the used in the surrogate training. The MI and SER results tested on the laser rate equations are shown as a function of P_{rec} in Fig. 11. Based on the figure, the AE delivers the best SER and MI performance overall, hinting that the optimization of I_{bias} level could have a higher impact on performance than the equalization in certain cases. This is more accentuated on the lower R_s than the higher ones, where the waveform distortion worsens the SNR, giving equalization a higher relative impact. Another interesting metric is the optimal I_{bias} obtained by the AE, resulting in $\{62.31, 69.31, 70.30\}$ mA at $\{15, 20, 25\}$ Gbaud, respectively. This trend provides interesting insight on the relation between the R_s and the optimal I_{bias} conditions. For the R_s analyzed, the E2E approaches show a clear performance advantage over the BL

and RX-only optimization. This is expected, given that the lack of nonlinearity in the latter makes the complete compensation of the DML-induced distortion infeasible at high symbol rates. The better performance of the E2E approaches serves as a further validation of the surrogate, as a poor model of the DML could lead to low performance when tested on the rate equations.

7. CONCLUSION

We propose a novel end-to-end, directly modulated laser optimization approach using a differentiable data-driven model as laser surrogate, allowing the propagation of gradients between transmitter and receiver. The surrogate is built based on the laser rate equations using various bias and peak-to-peak current values, in order to make it robust to such values. We compare different system architectures with conventional receiver-side optimization, varying the received optical power and the symbol rate of the simulation. The proposed autoencoder approach including bias and peak-to-peak current optimization shows significant performance gain compared to its receiver-side counterpart, showcasing the potential of end-to-end approaches in the optimization of directly modulated laser systems.

FUNDING

The Villum Fonden (VI-POPCOM VIL54486) and Villum YIP OPTIC-AI (no. VIL29334) projects are acknowledged.

REFERENCES

- N.-P. Diamantopoulos, T. Fujii, S. Yamaoka, H. Nishi, K. Takeda, T. Tsuchizawa, T. Segawa, T. Kakitsuka, and S. Matsuo, "60 GHz Bandwidth Directly Modulated Membrane III-V Lasers on SiO₂/Si," *J. Light. Technol.* **40**, 3299–3306 (2022).
- J. Huang, C. Li, R. Lu, L. Li, and Z. Cao, "Beyond the 100 Gbaud Directly Modulated Laser for Short Reach Applications," *J. Semicond.* **42**, 041306 (2021).
- D. Che and X. Chen, "Modulation Format and Digital Signal Processing for IM-DD Optics at Post-200G Era," *J. Light. Technol.* **42**, 588–605 (2024).
- M. S. Alam, R. Maram, K. A. Shahriar, P. Ricciardi, and D. V. Plant, "Chirped Managed Laser for Multilevel Modulation Formats: A Semi-analytical Approach for Efficient Filter Design," *J. Light. Technol.* pp. 1–11 (2023).
- L. A. Coldren, S. W. Corzine, and M. L. Mashanovitch, *Diode Lasers and Photonic Integrated Circuits* (John Wiley & Sons, 2012).
- X. Pang, T. Salgals, H. Louchet, D. Che, M. Gruen, Y. Matsui, T. Dippon, R. Schatz, M. Joharifar, B. Krüger, F. Pittala, Y. Fan, A. Udalcovs, L. Zhang, X. Yu, S. Spolitis, V. Bobrovs, S. Popov, and O. Ozolins, "200 Gb/s Optical-Amplifier-Free IM/DD Transmissions Using a Directly Modulated O-Band DFB+R Laser Targeting LR Applications," *J. Light. Technol.* **41**, 3635–3641 (2023).
- G. V. Rajeswari, M. Moehrl, F. Ehrensack, U. Troppenz, A. Sigmund, and M. Schell, "Novel >57 GHz bandwidth O-band InGaAlAs MQW RW DFB," in *Novel In-Plane Semiconductor Lasers XXII*, vol. 12440 A. A. Belyanin and P. M. Smowton, eds., International Society for Optics and Photonics (SPIE, 2023), p. 1244007.
- S. Yamaoka, N.-P. P. Diamantopoulos, H. Nishi, T. Fujii, K. Takeda, T. Hiraki, S. Kanazawa, T. Kakitsuka, and S. Matsuo, "Uncooled 100-Gbaud Directly Modulated Membrane Lasers on SiC Substrate," *J. Light. Technol.* **41**, 3389–3396 (2023).
- A. G. Reza, M. T. Costas, C. Browning, F. D. Otero, and L. Barry, "67.5 Gbit/s PAM-8 Signal Transmissions Over 25-km SMF With a 1550-nm 10G-Class DML Using Machine Learning," in *Conference on Lasers and Electro-Optics*, (Optica Publishing Group, 2022), p. SM3J.4.
- S. Hernandez, O. Jovanovic, C. Peucheret, F. D. Ros, and D. Zibar, "Differentiable Machine Learning-Based Modeling for Directly-Modulated Lasers," *IEEE Photonics Technol. Lett.* **36**, 266–269 (2024).
- S. Li, X. Jin, Y. Xuan, X. Zhou, W. Chen, Y.-X. Wang, and X. Yan, "Enhancing the Locality and Breaking the Memory Bottleneck of Transformer on Time Series Forecasting," in *Proceedings of the 33rd International Conference on Neural Information Processing Systems*, (2019).
- M. Srinivasan, J. Song, A. Grabowski, K. Szczerba, H. K. Iversen, M. N. Schmidt, D. Zibar, J. Schröder, A. Larsson, C. Häger, and H. Wymeersch, "End-to-End Learning for VCSEL-Based Optical Interconnects: State-of-the-Art, Challenges, and Opportunities," *J. Light. Technol.* **41**, 3261–3277 (2023).
- L. Minelli, F. Forghieri, A. Shahpari, T. Shao, and R. Gaudino, "TDECQ optimization of VCSEL-MMF nonlinear Digital Pre-Distorters using End-to-end Learning," in *European Conference on Optical Communication (ECOC)*, (2023), p. Th.B.5.6.
- F. A. Aoudia and J. Hoydis, "Model-Free Training of End-to-End Communication Systems," *IEEE J. on Sel. Areas Commun.* **37**, 2503–2516 (2019).
- M. P. Yankov, O. Jovanovic, D. Zibar, and F. D. Ros, "Recent Advances in Constellation Optimization for Fiber-optic Channels," in *European Conference on Optical Communication (ECOC) 2022*, (Optica Publishing Group, 2022), p. Mo3D.4.
- T. O'Shea and J. Hoydis, "An Introduction to Deep Learning for the Physical Layer," *IEEE Transactions on Cogn. Commun. Netw.* **3**, 563–575 (2017).
- I. Goodfellow, Y. Bengio, and A. Courville, *Deep Learning* (MIT Press, 2016).
- V. Oliari, B. Karanov, S. Goossens, G. Liga, O. Vassilieva, I. Kim, P. Palacharla, C. Okonkwo, and A. Alvarado, "Hybrid Geometric and Probabilistic Shaping; Is It Really Necessary?" in *Optica Advanced Photonics Congress 2022*, (2022), p. SpTu1J.4.
- A. Soleimanzade, M. Ardakani, and H. Ebrahimzad, "Optimization of the Non-Linearity Tolerant 4D Geometric Shaped Constellations for Optical Fiber Communication Systems Using Neural Networks," *J. Light. Technol.* **42**, 670–680 (2024).
- E. Sillekens, G. Liga, D. Lavery, P. Bayvel, and R. I. Killey, "High-Cardinality Geometrical Constellation Shaping for the Nonlinear Fibre Channel," *J. Light. Technol.* **40**, 6374–6387 (2022).
- O. Jovanovic, F. Da Ros, D. Zibar, and M. P. Yankov, "Geometric Constellation Shaping for Fiber-Optic Channels via End-to-End Learning," *J. Light. Technol.* **41**, 3726–3736 (2023).
- S. Yamaoka, N.-P. Diamantopoulos, H. Nishi, R. Nakao, T. Fujii, K. Takeda, T. Hiraki, T. Tsurugaya, S. Kanazawa, H. Tanobe, T. Kakitsuka, T. Tsuchizawa, F. Koyama, and S. Matsuo, "Directly modulated membrane lasers with 108 GHz bandwidth on a high-thermal-conductivity silicon carbide substrate," *Nat. Photonics* **15**, 28–35 (2021).
- T. Koch and J. Bowers, "Nature of Wavelength Chirping in Directly Modulated Semiconductor Lasers," *Electron. Lett.* **20**, 1038–1040 (1984).
- A. Villafranca, J. Lasobras, and I. Garces, "Precise Characterization of the Frequency Chirp in Directly Modulated DFB Lasers," in *2007 Spanish Conference on Electron Devices*, (2007), pp. 173–176.
- Y. Mao, Z. Ren, L. Guo, H. Wang, R. Zhang, Y. Huang, D. Lu, Q. Kan, C. Ji, and W. Wang, "Modulation Bandwidth Enhancement in Distributed Reflector Laser Based on Identical Active Layer Approach," *IEEE Photonics J.* **10** (2018).
- S. Sulikhah, S. L. Lee, and H. W. Tsao, "Improvement on Direct Modulation Responses and Stability by Partially Corrugated Gratings Based DFB Lasers With Passive Feedback," *IEEE Photonics J.* **13**, 1–14 (2021).
- Y. Matsui, R. Schatz, T. Pham, W. A. Ling, G. Carey, H. M. Daghighian, D. Adams, T. Sudo, and C. Roxlo, "55 GHz Bandwidth Distributed Reflector Laser," *J. Light. Technol.* **35**, 397–403 (2017).
- D. Che, Y. Matsui, R. Schatz, R. Rodes, F. Khan, M. Kwakernaak, and T. Sudo, "200-Gb/s Direct Modulation of a 50-GHz Class Laser With Advanced Digital Modulations," *J. Light. Technol.* **39**, 845–852 (2021).
- U. Feiste, "Optimization of modulation bandwidth in DBR lasers with detuned Bragg reflectors," *IEEE J. Quantum Electron.* **34**, 2371–2379 (1998).

30. M. Chaciński and R. Schatz, "Impact of Losses in the Bragg Section on the Dynamics of Detuned Loaded DBR Lasers," *IEEE J. Quantum Electron.* **46**, 1360–1367 (2010).
31. Y. Matsui, R. Schatz, D. Che, F. Khan, M. Kwakernaak, and T. Sudo, "Low-chirp Isolator-free 65-GHz-bandwidth Directly Modulated Lasers," *Nat. Photonics* **15**, 59–63 (2021).
32. P. Bardella and I. Montrosset, "A New Design Procedure for DBR Lasers Exploiting the Photon–Photon Resonance to Achieve Extended Modulation Bandwidth," *IEEE J. Sel. Top. Quantum Electron.* **19**, 1502408–1502408 (2013).
33. G. Morthier, R. Schatz, and O. Kjebon, "Extended Modulation Bandwidth of DBR and External Cavity Lasers by Utilizing a Cavity Resonance for Equalization," *IEEE J. Quantum Electron.* **36**, 1468–1475 (2000).
34. S. Guan, Y. Zhang, J. Zheng, J. Su, Z. Sun, L. Lu, T. Fang, L. Li, R. Xiao, Y. Shi, and X. Chen, "Modulation Bandwidth Enhancement and Frequency Chirp Suppression in Two-Section DFB Laser," *J. Light. Technol.* **40**, 7383–7389 (2022).
35. K. Shinohara, R. Miyagoshi, Y. Suzuki, R. Suzuki, G. Sakaino, M. Shimada, and K. Matsumoto, "106-Gbps PAM4 Operation at an Extinction Ratio above 3.5 dB using a Conventional Buried-Heterostructure Directly Modulated Laser," in *Optical Fiber Communication Conference (OFC) 2023*, (2023), p. M2D.6.
36. S. Ohno, M. Onga, T. Nakajima, A. Nakanishi, N. Sasada, S. Tanaka, R. Nakajima, and K. Naoe, "10-km Transmission of 106-Gb/s PAM4 with Directly Modulated DFB Lasers in the CWDM Range," in *Optical Fiber Communication Conference (OFC) 2023*, (2023), p. M2D.7.
37. X. Zhu, J. Guo, H. Li, Z. Li, D. Zhou, L. Zhao, W. Wang, and S. Liang, "High Speed Directly Modulated DFB Lasers Having MQW Based Passive Reflectors," *IEEE Photonics Technol. Lett.* **35**, 333–336 (2023).
38. H.-T. Cheng, Y.-C. Yang, T.-H. Liu, and C.-H. Wu, "Recent Advances in 850 nm VCSELs for High-Speed Interconnects," *Photonics* **9** (2022).
39. M. Hoser, W. Kaiser, D. Quandt, J. Bueno, S. Sainteny, and S. Eitel, "Highly Reliable 106 Gb/s PAM-4 850 nm Multi-Mode VCSEL for 800G Ethernet Applications," in *Optical Fiber Communication Conference (OFC) 2022*, (2022), p. Tu2D.5.
40. D. Wu, X. Yu, H. Wu, W. Fu, and M. Feng, "Single-mode 850nm VCSELs Demonstrate 96 Gb/s PAM4 OM4 Fiber Link for Extended Reach to 1km," in *Optical Fiber Communication Conference (OFC) 2022*, (2022), p. W2A.7.
41. J. Wang, Y. Ji, Z. Yang, H. Hu, J. Chen, H. Li, F. Li, S. Li, J. Kapraun, C. Shen, and C. J. Chang-Hasnain, "300-m Multimode Fiber Transmission of 106Gbps PAM-4 Using 850nm High-Contrast-Grating Few-mode VCSELs," in *European Conference on Optical Communication (ECOC)*, (2022), p. Tu3E.3.
42. C. Ge, L. Dong, X. Gu, and F. Koyama, "1060nm Single-mode Intracavity Metal-aperture VCSEL for over 2km Standard 1300nm SMF Transmission," in *CLEO 2023*, (2023), p. STh4Q.2.
43. J. Chi, X. Li, C. Niu, and J. Zhao, "Output Optical Power Enhancement of Push-Pull Modulated DFB Laser With Asymmetric Structure," *IEEE Photonics J.* **15**, 1–8 (2023).
44. D. Che, Y. Matsui, X. Chen, R. Schatz, and P. Iannone, "400-Gb/s Direct Modulation using a DFB+R Laser," *Opt. Lett.* **45**, 3337–3339 (2020).
45. J. Chi, C. Niu, and J. Zhao, "Parameter Extraction For Quantum Well DFB Lasers Based on 1D Traveling Wave Model," *IEEE Photonics J.* **14**, 1–8 (2022).
46. L. Bjerkan, A. Royset, L. Hafskjaer, and D. Myhre, "Measurement of Laser Parameters for Simulation of High-Speed Fiberoptic Systems," *J. Light. Technol.* **14**, 839–850 (1996).
47. J. Cartledge and R. Srinivasan, "Extraction of DFB Laser Rate Equation Parameters for System Simulation Purposes," in *Conference Proceedings LEOS'96 9th Annual Meeting IEEE Lasers and Electro-Optics Society*, vol. 2 (1996), pp. 248–249.
48. I. Tomkos, I. Roudas, R. Hesse, N. Antoniadis, A. Boskovic, and R. Vodhanel, "Extraction of Laser Rate Equations Parameters for Representative Simulations of Metropolitan-area Transmission Systems and Networks," *Opt. Commun.* **194**, 109–129 (2001).
49. A. Marchisio, E. Ghillino, V. Curri, A. Carena, and P. Bardella, "Particle Swarm Optimization-assisted Approach for the Extraction of VCSEL Model Parameters," *Opt. Lett.* **49**, 125–128 (2024).
50. S. J. Zhang, N. H. Zhu, E. Y. B. Pun, and P. S. Chung, "Rate-equation-based Circuit Model of High-speed Semiconductor Lasers," *Microw. Opt. Technol. Lett.* **49**, 539–542 (2007).
51. J. Butcher, *Numerical Methods for Ordinary Differential Equations* (Wiley Blackwell, 2016).
52. A. Griewank, "A mathematical view of automatic differentiation," *Acta Numer.* **12**, 321–398 (2003).
53. A. G. Baydin, B. A. Pearlmutter, A. A. Radul, and J. M. Siskind, "Automatic differentiation in machine learning: a survey," *J. Mach. Learn. Res.* **18**, 5595–5637 (2017).
54. W. W. Feng and N. H. Zhu, "Analysis of Chirp Characteristics of DFB Lasers and Integrated Laser-modulators," *Opt. Quantum Electron.* **36**, 1237–1245 (2004).
55. Q. Ding, Q. Yang, J. Li, C. Gu, Z. Li, X. Tan, F. Gao, X. Chen, and Q. Niu, "Efficient and systematic parameter extraction based on rate equations by DFB equivalent circuit model," *Opt. Express* **31**, 40604–40619 (2023).
56. J. Katz, S. Margalit, C. Harder, D. Wilt, and A. Yariv, "The Intrinsic Electrical Equivalent Circuit of a Laser Diode," *IEEE J. Quantum Electron.* **17**, 4–7 (1981).
57. I. Habermayer, "Nonlinear Circuit Model for Semiconductor Lasers," *Opt. Quantum Electron.* **13**, 461–468 (1981).
58. R. S. Tucker, "Circuit model of double-heterojunction laser below threshold," *IEEE Proc. I (Solid-State Electron Devices)* **128**, 101–106(5) (1981).
59. S. Ghoniemy, L. MacEachern, and S. Mahmoud, "Extended Robust Semiconductor Laser Modeling for Analog Optical Link Simulations," *IEEE J. Sel. Top. Quantum Electron.* **9**, 872–878 (2003).
60. A. Horri, S. Z. Mirmoeini, and R. Faez, "The Noise Equivalent Circuit Model of Quantum-dot Lasers," *J. Russ. Laser Res.* **33**, 217–226 (2012).
61. E. Mortazy, V. Ahmadi, and M. Moravvej-Farshi, "An Integrated Equivalent Circuit Model for Relative Intensity Noise and Frequency Noise Spectrum of a Multimode Semiconductor Laser," *IEEE J. Quantum Electron.* **38**, 1366–1371 (2002).
62. L. Ljung, *System Identification* (John Wiley and Sons, Ltd, 2017), chap. 5 - Models for Time-varying and Nonlinear Systems, pp. 140–161.
63. O. Nelles, *Nonlinear System Identification From Classical Approaches to Neural Networks, Fuzzy Models, and Gaussian Processes* (Springer Cham, 2020), 2nd ed.
64. T. Jakaša, I. Andročec, and P. Sprčić, "Electricity Price Forecasting — ARIMA Model Approach," in *2011 8th International Conference on the European Energy Market (EEM)*, (2011), pp. 222–225.
65. D. R. Irmawati, R. M. Atok, and Suhartono, "Hybrid Singular Spectrum Analysis-ARIMA Modelling for Direct and Indirect Forecasting of Farmer's Term of Trade in East Java," in *2018 International Conference on Information and Communications Technology (ICOIACT)*, (2018), pp. 889–894.
66. S. Zhang and Y. Liu, "Forecasting Model of Total Import and Export based on ARIMA Algorithm Optimized by BP Neural Network," in *2023 IEEE 3rd International Conference on Data Science and Computer Application (ICDSCA)*, (2023), pp. 1534–1538.
67. L. Ljung, C. Andersson, K. Tiels, and T. B. Schön, "Deep Learning and System Identification," 21st IFAC World Congr. **53**, 1175–1181 (2020).
68. J. Schoukens and L. Ljung, "Nonlinear System Identification: A User-Oriented Road Map," *IEEE Control. Syst. Mag.* **39**, 28–99 (2019).
69. H.-Y. Chen, C.-C. Wei, C.-Y. Lin, L.-W. Chen, I.-C. Lu, and J. Chen, "Frequency- and Time-domain Nonlinear Distortion Compensation in High-speed OFDM-IMDD LR-PON with High Loss Budget," *Opt. Express* **25**, 5044–5056 (2017).
70. Y. Xu, L. Huang, W. Jiang, L. Xue, W. Hu, and L. Yi, "Automatic Optimization of Volterra Equalizer With Deep Reinforcement Learning for Intensity-Modulated Direct-Detection Optical Communications," *J. Light. Technol.* **40**, 5395–5406 (2022).
71. N. Stojanovic, F. Karinou, Z. Qiang, and C. Prodaniuc, "Volterra and

- Wiener Equalizers for Short-Reach 100G PAM-4 Applications," *J. Light. Technol.* **35**, 4583–4594 (2017).
72. F. P. Guiomar, S. B. Amado, C. S. Martins, and A. N. Pinto, "Time-Domain Volterra-Based Digital Backpropagation for Coherent Optical Systems," *J. Light. Technol.* **33**, 3170–3181 (2015).
 73. S. Elliott, "8 - Active Control of Nonlinear Systems," in *Signal Processing for Active Control*, (Academic Press, 2001), Signal Processing and its Applications, pp. 367–409.
 74. K. L. J. Tsimbinos, "Computational Complexity of Volterra based Nonlinear Compensators," *Electron. Lett.* **32**, 852–854(2) (1996).
 75. J. Tsimbinos and K. Lever, "The Computational Complexity of Nonlinear Compensators based on the Volterra Inverse," in *Proceedings of 8th Workshop on Statistical Signal and Array Processing*, (1996), pp. 387–390.
 76. M. J. Korenberg, S. B. Bruder, and P. J. McLlroy, "Exact Orthogonal Kernel Estimation from Finite Data Records: Extending Wiener's Identification of Nonlinear Systems," *Annals Biomed. Eng.* **16**, 201–214 (1988).
 77. E. Thomas, J. van Hemmen, and W. Kistler, "Calculation of Volterra Kernels for Solutions of Nonlinear Differential Equations," *Siam J. on Appl. Math.* **61** (2000).
 78. S. Orcioni, M. Pirani, and C. Turchetti, "Advances in Lee-Schetzen Method for Volterra Filter Identification," *Multidimens. Syst. Signal Process.* **16**, 265–284 (2005).
 79. A. Wills, T. B. Schön, L. Ljung, and B. Ninness, "Identification of Hammerstein–Wiener Models," *Automatica.* **49**, 70–81 (2013).
 80. X. Liu, Y. Fan, Y. Zhang, M. Cai, L. Liu, L. Yi, W. Hu, and Q. Zhuge, "Fusing Physics to Fiber Nonlinearity Model for Optical Networks Based on Physics-Guided Neural Networks," *J. Light. Technol.* **40**, 5793–5802 (2022).
 81. Y. Song, Y. Zhang, C. Zhang, J. Li, M. Zhang, and D. Wang, "PINN for Power Evolution Prediction and Raman Gain Spectrum Identification in C+L-Band Transmission System," in *Optical Fiber Communication Conference (OFC) 2023*, (2023), p. Th1F.5.
 82. U. C. de Moura, D. Zibar, A. Margareth Rosa Brusin, A. Carena, and F. Da Ros, "Fiber-Agnostic Machine Learning-Based Raman Amplifier Models," *J. Light. Technol.* **41**, 83–95 (2023).
 83. D. Wang, Y. Song, J. Li, J. Qin, T. Yang, M. Zhang, X. Chen, and A. C. Boucouvalas, "Data-driven Optical Fiber Channel Modeling: A Deep Learning Approach," *J. Light. Technol.* **38**, 4730–4743 (2020).
 84. A. Waibel, T. Hanazawa, G. Hinton, K. Shikano, and K. J. Lang, "Phoneme Recognition Using Time-Delay Neural Networks," *Readings Speech Recognit.* pp. 393–404 (1990).
 85. A. G. Reza and J.-K. K. Rhee, "Nonlinear Equalizer Based on Neural Networks for PAM-4 Signal Transmission Using DML," *IEEE Photonics Technol. Lett.* **30**, 1416–1419 (2018).
 86. Y. LeCun and Y. Bengio, *Convolutional Networks for Images, Speech, and Time Series* (MIT Press, 1998), p. 255–258.
 87. K. Cho, B. van Merriënboer, C. Gulcehre, F. Bougares, H. Schwenk, and Y. Bengio, "Learning phrase representations using RNN encoder-decoder for statistical machine translation," in *Conference on Empirical Methods in Natural Language Processing (EMNLP 2014)*, (2014).
 88. S. Hochreiter and J. Schmidhuber, "Long Short-Term Memory," *Neural Comput.* **9**, 1735–1780 (1997).
 89. T. K. Rusch and S. Mishra, "UniCORNN: A recurrent model for learning very long time dependencies," in *Proceedings of the 38th International Conference on Machine Learning*, vol. 139 M. Meila and T. Zhang, eds. (2021), pp. 9168–9178.
 90. A. Vaswani, N. Shazeer, N. Parmar, J. Uszkoreit, L. Jones, A. N. Gomez, L. u. Kaiser, and I. Polosukhin, "Attention is All you Need," in *Advances in Neural Information Processing Systems*, vol. 30 I. Guyon, U. V. Luxburg, S. Bengio, H. Wallach, R. Fergus, S. Vishwanathan, and R. Garnett, eds. (2017).
 91. N. Zhang, H. Yang, Z. Niu, L. Zheng, C. Chen, S. Xiao, and L. Yi, "Transformer-Based Long Distance Fiber Channel Modeling for Optical OFDM Systems," *J. Light. Technol.* **40**, 7779–7789 (2022).
 92. Y. Zhu, J. Ye, L. Yan, T. Zhou, P. Li, X. Zou, and W. Pan, "Transformer-Based High-Fidelity Modeling Method for Radio Over Fiber Link," *J. Light. Technol.* **41**, 2657–2665 (2023).
 93. B. Li, Q. Du, T. Zhou, Y. Jing, S. Zhou, X. Zeng, T. Xiao, J. Zhu, X. Liu, and M. Zhang, "ODE Transformer: An Ordinary Differential Equation-Inspired Model for Sequence Generation," in *Proceedings of the 60th Annual Meeting of the Association for Computational Linguistics (Volume 1: Long Papers)*, S. Muresan, P. Nakov, and A. Villavicencio, eds. (2022), pp. 8335–8351.
 94. A. Gatto, M. Rapisarda, P. Parolari, and P. Boffi, "Discrete Multitone Modulation for Short-Reach Mode Division Multiplexing Transmission," *J. Light. Technol.* **37**, 5185–5192 (2019).
 95. G. Böcherer, P. Schulte, and F. Steiner, "Probabilistic Shaping and Forward Error Correction for Fiber-Optic Communication Systems," *J. Light. Technol.* **37**, 230–244 (2019).
 96. D. Che and W. Shieh, "Approaching the Capacity of Colored-SNR Optical Channels by Multicarrier Entropy Loading," *J. Light. Technol.* **36**, 68–78 (2018).
 97. D. Kim and H. Kim, "Capacity-achieving Symbol Distributions for Directly Modulated Laser and Direct Detection Systems," *Opt. Express* **31**, 12609–12623 (2023).
 98. N.-P. Diamantopoulos, H. Yamazaki, S. Yamaoka, M. Nagatani, H. Nishi, H. Tanobe, R. Nakao, T. Fujii, K. Takeda, T. Kakitsuka, H. Wakita, M. Ida, H. Nosaka, F. Koyama, Y. Miyamoto, and S. Matsuo, ">100-GHz Bandwidth Directly-Modulated Lasers and Adaptive Entropy Loading for Energy-Efficient >300-Gbps/λ IM/DD Systems," *J. Light. Technol.* **39**, 771–778 (2021).
 99. C. Kottke, C. Caspar, V. Jungnickel, R. Freund, M. Agustin, and N. N. Ledentsov, "High Speed 160 Gb/s DMT VCSEL Transmission Using Pre-equalization," in *Optical Fiber Communication Conference*, (Optica Publishing Group, 2017), p. W41.7.
 100. D. Dasalukunte, F. Rusek, and V. Owall, "Multicarrier Faster-Than-Nyquist Transceivers: Hardware Architecture and Performance Analysis," *IEEE Transactions on Circuits Syst. I: Regul. Pap.* **58**, 827–838 (2011).
 101. N. Bamiedakis, D. G. Cunningham, and R. V. Penty, "Linearisation Method of DML-Based Transmitters for Optical Communications Part I: Theory and Simulation Studies," *J. Light. Technol.* **39**, 5815–5827 (2021).
 102. Q.-A. Ding, Huixin-Liu, X. Cheng, X.-J. Wang, W. Huang, L. Du, G. Zhu, L. Zheng, and Q. Yang, "Suppressing DFB Lasers Relaxation Oscillations by High-Order Continuous Shaping Current With CNN Prediction," *IEEE J. Quantum Electron.* **59**, 1–11 (2023).
 103. Z. Feng, N. Li, W. Li, P. He, M. Luo, Q. Hu, L. Huang, and Y. Jiang, "A Simplified Volterra Equalizer Based on System Characteristics for Direct Modulation Laser (DML)-Based Intensity Modulation and Direct Detection (IM/DD) Transmission Systems," *Photonics.* **10** (2023).
 104. N.-P. Diamantopoulos, H. Nishi, W. Kobayashi, K. Takeda, T. Kakitsuka, and S. Matsuo, "On the Complexity Reduction of the Second-Order Volterra Nonlinear Equalizer for IM/DD Systems," *J. Light. Technol.* **37**, 1214–1224 (2019).
 105. Z. Xu, C. Sun, T. Ji, H. Ji, and W. Shieh, "Cascade Recurrent Neural Network Enabled 100-Gb/s PAM4 Short-Reach Optical Link Based on DML," in *Optical Fiber Communication Conference (OFC) 2020*, (2020), p. W2A.45.
 106. F. Tian and C. Yang, "Deep Belief Network-Hidden Markov Model-based Nonlinear Equalizer for VCSEL based Optical Interconnect," *Sci. China Inf. Sci.* **63** (2020).
 107. F. A. Aoudia and J. Hoydis, "End-to-End Learning of Communications Systems Without a Channel Model," in *2018 52nd Asilomar Conference on Signals, Systems, and Computers*, (2018), pp. 298–303.
 108. M. Srinivasan, J. Song, C. Häger, K. Szczerba, H. Wymeersch, and J. Schröder, "Learning Optimal PAM Levels for VCSEL-based Optical Interconnects," in *European Conference on Optical Communication (ECOC) 2022*, (2022), p. We2C.3.
 109. L. Minelli, F. Forghieri, T. Shao, A. Shahpari, and R. Gaudino, "TDECQ-Based Optimization of Nonlinear Digital Pre-Distorters for VCSEL-MMF Optical Links Using End-to-End Learning," *J. Light. Technol.* **42**, 621–635 (2024).
 110. B. Karanov, M. Chagnon, F. Thouin, T. A. Eriksson, H. Bülow, D. Lavery,

- P. Bayvel, and L. Schmalen, "End-to-End Deep Learning of Optical Fiber Communications," *J. Light. Technol.* **36**, 4843–4855 (2018).
111. R. T. Jones, T. A. Eriksson, M. P. Yankov, and D. Zibar, "Deep Learning of Geometric Constellation Shaping Including Fiber Nonlinearities," in *2018 European Conference on Optical Communication (ECOC)*, (2018).
112. P. Freire, S. Srivallapanondh, B. Spinnler, A. Napoli, N. Costa, J. E. Prilepsky, and S. K. Turitsyn, "Computational Complexity Optimization of Neural Network-Based Equalizers in Digital Signal Processing: A Comprehensive Approach," *J. Light. Technol.* pp. 1–25 (2024).
113. J. Cartledge and G. Burley, "The effect of laser chirping on lightwave system performance," *J. Light. Technol.* **7**, 568–573 (1989).
114. J. Cartledge and R. Srinivasan, "Extraction of dfb laser rate equation parameters for system simulation purposes," *J. Light. Technol.* **15**, 852–860 (1997).